X-ray powder diffraction line broadening analysis and magnetism of interacting ferrite nanoparticles obtained from acetylacetonato complexes

2005 J. Phys.: Condens. Matter 17 4285

(http://iopscience.iop.org/0953-8984/17/27/005)

INSTITUTE OF PHYSICS PUBLISHING JOURNAL OF PHYSICS: CONDENSED MATTER

J. Phys.: Condens. Matter **17** (2005) 4285–4299 doi:10.1088/0953-8984/17/27/005

X-ray powder diffraction line broadening analysis and magnetism of interacting ferrite nanoparticles obtained from acetylacetonato complexes

A Kremenovic[1,2,5], B Antic[1], V Spasojevic[1], M Vucinic-Vasic[3], Z Jaglicic[4], J Pirnat[4] and Z Trontelj[4]

[1] Condensed Matter Physics Laboratory, The 'Vinca' Institute, POB 522, 11001 Belgrade, Serbia and Montenegro
[2] Faculty of Mining and Geology, Laboratory for Crystallography, University of Belgrade, POB 162, 11001 Belgrade, Serbia and Montenegro
[3] Faculty of Technical Sciences, University of Novi Sad, Trg D Obradovica 6, 21000 Novi Sad, Serbia and Montenegro
[4] Institute of Mathematics, Physics and Mechanics, Jadranska 19, 1000 Ljubljana, Slovenia

E-mail: akremen@eunet.yu

Received 3 March 2005, in final form 7 June 2005
Published 24 June 2005
Online at stacks.iop.org/JPhysCM/17/4285

Abstract

A study of the microstructures and magnetic properties of nanosize Zn ferrite ($ZnFe_2O_4$), Mn ferrite ($MnFe_2O_4$), and the cation deficit Zn–Mn ferrites $Zn_{0.70}Mn_{0.23}Fe_{1.89}O_4$ (S1), $Zn_{0.41}Mn_{0.50}Fe_{1.84}O_4$ (S2) and $Zn_{0.18}Mn_{0.67}Fe_{1.85}O_4$ (S3) was performed. The crystallite size for all samples was determined by x-ray powder diffraction (XRPD) analysis using four different methods, and was close to the particle size found from transmission electron microphotography. Among different methods of XRPD line broadening analysis it seems that the cubic harmonic function method is more precise and reliable than the Warren–Averbach and simplified integral breadth methods. $M(T)$ and $M(H)$ magnetization curves at different fields/temperatures indicate superparamagnetic behaviour of the samples. Asymmetric hysteresis loops and differences in coercive fields, H_{C-}(FC) − H_{C-}(ZFC), are discussed by both the core/shell model of nanoparticles and spin canting. The magnetic measurements with a maximum in the FC magnetization branches, the difference in M/M_S versus H/T curves above T_{max} (temperature of maximum in ZFC magnetization), the nonlinearity in H_C versus $T^{1/2}$, the remanence/saturation ratio value, M_R/M_S and observation of the Almeida–Thouless line for low-field magnetization data (T_{max} versus $H^{2/3}$) indicate that the samples consist of an interacting ferrite nanoparticle ensemble.

(Some figures in this article are in colour only in the electronic version)

[5] Author to whom any correspondence should be addressed.

1. Introduction

Nanoparticles have unique physical properties as a consequence of dimensional reduction. Their properties are either significantly modified (e.g. coercive field, Curie temperature, saturation magnetization) or new ones that are not present in the bulk. Below some critical dimension, magnetic particles become single domain and show superparamagnetic (SPM) behaviour [1–3]. The magnetic properties of such particles are well described by the Néel model [4], where the magnetic anisotropy energy E_A is a key factor in determining the magnetic behaviour of nanoparticles. Below the blocking temperature T_B, the thermal energy is not strong enough to overcome E_A, and particle moments are blocked. Above T_B, the thermal energy and applied field move the magnetization direction of the nanoparticles away from their easy axis and particles show superparamagnetism. In the Néel model the particles are considered to be non-interacting. On the other hand, when interparticle interactions are strong enough, a magnetic phase transition from a superparamagnetic to a collective superspin glass (SSG) occurs [5, 6]. However, in real nanomaterials the magnetic properties are governed both by the intrinsic magnetic anisotropy energy and interparticle interactions.

Magnetism is an area where microstructure is vital but poorly understood at the microscopic level. From the technical point of view, the magnetic characteristics of materials crucially depend on their microstructure [7]. A similar situation exists in conventional transition metal magnets, where control of the microstructure is the central task in the development of alloy systems with desirable technical properties (coercivity, remanence and permeability). Experimental studies of nanosize materials are often concerned with the influence of particle size and its distribution on magnetic properties, such as blocking temperature, coercivity, remanence and saturation magnetization. To the best of our knowledge, no systematic studies of the relationship between microstructure determined from diffraction data and the magnetic properties of nanoparticles have been made. Nowadays, progress in both instrumentation and data analysis facilitates systematic size–strain crystallographic studies, which together with magnetic measurements provide a better understanding of the above-mentioned relationships in nanomagnetism. This was one of the goals of the present study.

Cubic nanosize spinel ferrites with the general formula MFe_2O_4 are well known, important materials for applications such as high-density information storage media, drug delivery, medical diagnostics, ferrofluids, electronic devices, and catalysts [8, 9]. Also, nanometre scale ferrites are a current topic of basic research in nanomagnetism. In the unit cell of spinels, oxygen ions form close packing, with M^{2+} and Fe^{3+} ions distributed between tetrahedral A (8a) and octahedral B (16d) interstitial sites. In most cases ferrites with the spinel structure have $(M, Fe)_3O_4$ stoichiometry, where the cation/anion ratio is 3/4, although deviation from stoichiometry is possible [10, 11]. In cation-deficient spinels, the vacancies present lead to modification of the cation valence, thus influencing the physical properties. For example, an increase in the initial permeability of Zn–Mn ferrites with increasing non-stoichiometry [12], or a significant variation of permeability in Mg–Mn ferrites even for a small deviation of stoichiometry was found [13].

In a previous paper [11] we presented results on the cation distribution and size–strain analysis obtained by the Rietveld method in nanosized Zn and Mn ferrites, and also in the cation deficit Zn–Mn ferrites $Zn_{0.70}Mn_{0.23}Fe_{1.89}O_4$ (S1), $Zn_{0.41}Mn_{0.50}Fe_{1.84}O_4$ (S2) and $Zn_{0.18}Mn_{0.67}Fe_{1.85}O_4$ (S3) obtained by thermal decomposition of appropriate mixed complex compounds with acetylacetone (2,4-pentadione) ligands [11]. Our previous work was continued with the following aims:

(a) to analyse structural and microstructural data applying the Warren–Averbach and simplified integral breadth methods and to compare them with the results obtained using the cubic harmonic function method, and
(b) to study the magnetic properties of these samples by DC magnetization measurements.

2. Experimental section

2.1. Magnetization and TEM measurement

Zero-field-cooled (ZFC) and field-cooled (FC) magnetizations were measured in the temperature range 2–350 K, and in an applied field of 100 Oe, using an MPMS XL-5 SQUID magnetometer. Hysteresis loops were measured at 5 and 350 K for all samples. For sample S1 the hysteresis loops were also measured in different applied fields (50 Oe–2 kOe) and at different temperatures (2–80 K). The latter $M(T)$ measurements were made in both ZFC and FC regimes. In the FC regime the sample was cooled in a 50 kOe field down to low temperature, and measurement was made from 50 kOe up to −50 kOe, and vice versa.

Transmission electron microscopy (TEM) was performed on a Philips M400 equipment.

2.2. Size–strain microstructure analysis procedure

The x-ray line broadening was analysed by the Breadth computer programs [14]. The Breadth program calculates microstructural parameters according to the Warren–Averbach and simplified integral breadth methods [15, 16]. The x-ray line broadening of the hhh ($h = 1, \ldots, 5$) and $hh0$ ($h = 2, \ldots, 6$) reflections was analysed. Input data for the Breadth program, such as unit-cell parameters, peak positions ($2\theta_{\max}$), FWHM (full width half maximum) and Lorenz/Gauss mixing components (η), were taken from the output of the FullProf program given in [11].

3. Results and discussion

3.1. Size–strain microstructure analysis

At the beginning of this section we briefly summarize the results obtained in our previous study [11] on the cation distribution obtained by the Rietveld crystal structure refinement. The cation distribution in $ZnFe_2O_4$ was partially inverse with 14% of Zn^{2+} ions at octahedral 16d sites, while $MnFe_2O_4$ was a normal spinel. The cation distribution in non-stoichiometric $(Zn, Mn, Fe)_{3-\delta}O_4$ ($\delta = 0.18$–0.30) was found to be $(Zn_xMn_{y-\varepsilon})_{8a}\,[Fe_{z-\nu}]_{16d}$, with a random distribution of vacancies. Based on the refined occupation numbers for ternary samples [11], we calculated the vacancy concentrations. The parameters ε and ν were as follows: $\varepsilon = 0.07$, $\nu = 0.11$ for sample S1, $\varepsilon = 0.09$, $\nu = 0.16$ for S2 and $\varepsilon = 0.15$, $\nu = 0.15$ for S3. Non-stoichiometry in Zn–Mn ferrites was accompanied by a cation valence change, i.e. partial oxidation of Mn^{2+} to Mn^{4+} [11].

To analyse the influence of vacancies and other structural misfits on the magnetic behaviour of the spinels studied, it is important to define, as precisely as possible, the microstructure of the investigated samples. Therefore, in sections 3.1.1–3.1.3 we present, compare and discuss our obtained results, particularly the role of specimen preparation on the size–strain results, different size–strain analysis results and applied methods.

3.1.1. Role of specimen preparation on obtained size–strain results. The role of the specimen and the crystallite statistics for an x-ray powder diffraction (XRPD) experiment (experiment

involving intensity measurements) are very important. An increase of the data collection time showed no effect on the crystallite statistics. The number of crystallites that contribute to the diffraction spectrum is limited by their size, the volume of the specimen in the beam, and whether the specimen was moving during the measurements. There are a number of ways to increase this number for a given instrument. The easiest way is to reduce the crystallite size to dimensions around 1 μm, but this is not always possible. Therefore, the specimen size could be the limiting factor in the experiment. However, we prepared ultrafine powders of Zn–Mn ferrites with average grain sizes of a few hundred ångströms [11]. The intensities obtained in the XRPD patterns were reliable, as was proved by the low accuracy parameters for the Rietveld refinements (see table 1 in [11]). In this way, we were able to conclude that our profile analyses were accurate and reliable.

3.1.2. Comparison of size–strain analysis results. In order to analyse precisely and reliably the crystallites' size/strain relationship and their anisotropy in the nanoparticle samples under consideration we used four different methods for the x-ray diffraction line broadening analysis: Warren–Averbach and simplified integral breadth (incorporated in the Breadth computer program), as well as refinements of the TCH–pV parameter and cubic harmonic function methods (incorporated in the FullProf computer program). Previously we obtained [11] the size and strain of crystallites using the FullProf program which, for the sake of comparison, are shown in table 1. The same table also contains results obtained by the Breadth program for crystallite domain sizes a_3', surface-weighted $\langle D\rangle_{\rm S}$ and volume-weighted $\langle D\rangle_{\rm V}$. The volume-averaged domain sizes evaluated from the simplified integral-breadth method in the approximation of Cauchy–Cauchy $\langle D\rangle_{\rm CC}$, Cauchy–Gauss $\langle D\rangle_{\rm CG}$, and Gauss–Gauss $\langle D\rangle_{\rm GG}$ distribution of crystallites and strains are also given. The root mean square strains (RMSS) over the distances $\langle D\rangle_{\rm S/2}$, $(\langle\varepsilon^2\rangle^{1/2}_{\langle D\rangle{\rm S}/2})$, $\langle D\rangle_{\rm V/2}(\langle\varepsilon^2\rangle^{1/2}_{\langle D\rangle{\rm V}/2})$, $a_3'(\langle\varepsilon^2\rangle^{1/2}_{a_3'})$ and infinity $(\langle\varepsilon^2\rangle^{1/2}_{\rm Gauss})$ are also presented in table 1. The upper limits of strain from the simplified integral-breadth methods in the approximate Cauchy–Cauchy, $\langle\varepsilon^2\rangle^{1/2}_{\rm CC}$, Cauchy–Gauss, $\langle\varepsilon^2\rangle^{1/2}_{\rm CG}$ and Gauss–Gauss, $\langle\varepsilon^2\rangle^{1/2}_{\rm GG}$ distribution of crystallites and strains are also shown.

From the results obtained by the Breadth and FullProf programs, it could be concluded that in the binary spinels the crystallites are bigger in $ZnFe_2O_4$ than in $MnFe_2O_4$, while the RMSSs are lower in $ZnFe_2O_4$ than in $MnFe_2O_4$. The anisotropy of x-ray line broadening is significantly higher in the binary than in the ternary spinels S1, S2 and S3. The strain-induced x-ray line broadening anisotropy is about twice as high in $ZnFe_2O_4$ (21.4%) than in $MnFe_2O_4$ (10%). In the ternary samples the crystallites are a little bigger in S3 than in S1 and S2, while the RMSSs are a little higher in S2 and S3 than in S1. The anisotropy of x-ray line broadening decreases as the vacancy concentration δ increases: 13.3% for S1, 3.8% for S2 and 4.1% for S3. The average apparent crystallite size increases with increase of the cation deficit in the 8a tetrahedral position. Results obtained by the Breadth program indicate that the magnitude of broadening is given mostly by the Cauchy component. In figure 1, crystallite size and RMSS strain distributions are presented. As the crystallite size decreases the distribution pV becomes increasingly narrow, indicating a uniform crystallite distribution for a smaller crystallite size. The RMSS strain distribution over the distance L is more or less the same for all specimens. Between 50 and 1000 Å, which should be the limit for grain sizes (see the TEM results presented below), the RMSSs are between 0.003 and 0.0015. This is an indication that the prepared ultrafine ferrite powders are of a good crystallinity. Thus we were able to perform reliable diffraction experiments.

The four different methods are not in complete agreement. On a relative scale, the size–strain analysis results are in agreement. All methods indicate that the crystallite size and the

Table 1. The microstructure size–strain parameters for cation-deficient $Zn_xMn_yFe_zO_4$.

	$ZnFe_2O_4$		$Zn_{0.70}Mn_{0.23}Fe_{1.89}O_4$ (S1)		$Zn_{0.41}Mn_{0.50}Fe_{1.84}O_4$ (S2)		$Zn_{0.18}Mn_{0.67}Fe_{1.85}O_4$ (S3)		$MnFe_2O_4$	
Hkl	hhh	$hh0$	hhh	$hh0$	hhh	$hh0$	hhh	$hh0$	hhh	$hh0$
Warren–Averbach method										
a_3' (Å)	5.6	5.7	4.1	4.5	3.5	3.4	4.5	4.5	0.8	2.8
$\langle D\rangle_S$ (Å)	108 ± 3	103 ± 3	57 ± 1	61 ± 1	56 ± 1	57 ± 1	74 ± 1	71 ± 1	48 ± 1	46 ± 1
$\langle D\rangle_V$ (Å)	184 ± 4	179 ± 4	113 ± 3	121 ± 3	110 ± 2	113 ± 7	146 ± 4	140 ± 5	96 ± 2	91 ± 2
$\langle \varepsilon^2\rangle^{1/2}_{\langle D\rangle S/2} \times 10^3$	2.6 ± 0.1	2.5 ± 0.1	2.74 ± 0.05	2.60 ± 0.05	3.8 ± 0.1	3.93 ± 0.04	3.03 ± 0.06	3.05 ± 0.09	4.8 ± 0.1	4.8 ± 0.1
$\langle \varepsilon^2\rangle^{1/2}_{\langle D\rangle V/2} \times 10^3$	2.00 ± 0.09	1.92 ± 0.08	1.99 ± 0.03	1.89 ± 0.04	2.69 ± 0.07	2.83 ± 0.03	2.22 ± 0.04	2.23 ± 0.06	3.47 ± 0.08	3.49 ± 0.09
$\langle \varepsilon^2\rangle^{1/2}_{a_3'} \times 10^3$	7.8 ± 0.3	7.4 ± 0.3	7.0 ± 0.1	6.6 ± 0.1	10.6 ± 0.3	11.2 ± 0.1	8.4 ± 0.2	8.3 ± 0.2	14.0 ± 0.4	13.7 ± 0.4
$\langle \varepsilon^2\rangle^{1/2}_{Gauss} \times 10^3$	4.4 ± 0.6	5.0 ± 0.5	6.10 ± 0.08	6.15 ± 0.08	5.0 ± 0.1	6.9 ± 0.2	7.5 ± 0.2	7.9 ± 0.1	8.74 ± 0.06	9.07 ± 0.07
Simplified integral breadth method										
$\langle D\rangle_{CC}$ (Å)	218	222	124	137	128	141	176	176	121	116
$\langle D\rangle_{CG}$ (Å)	188	186	115	124	113	119	152	148	103	97
$\langle D\rangle_{GG}$ (Å)	184	182	114	123	111	116	148	145	100	94
$\langle \varepsilon^2\rangle^{1/2}_{CC} \times 10^3$	1.92	1.98	1.47	1.53	2.51	3.01	2.30	2.43	3.80	3.85
$\langle \varepsilon^2\rangle^{1/2}_{CG} \times 10^3$	2.61	2.59	2.57	2.47	3.64	3.98	3.14	3.19	5.02	5.00
$\langle \varepsilon^2\rangle^{1/2}_{GG} \times 10^3$	3.29	3.26	3.41	3.26	4.67	5.03	3.97	4.02	6.28	6.28
FullProf										
Average apparent size (Å) [11]	277(10)		146(7)		146(2)		204(1)		128(4)	
Average mixing strain $\times 10^3$ [11]	1.4(3)		1.5(2)		2.6(1)		2.4(1)		4.0(4)	

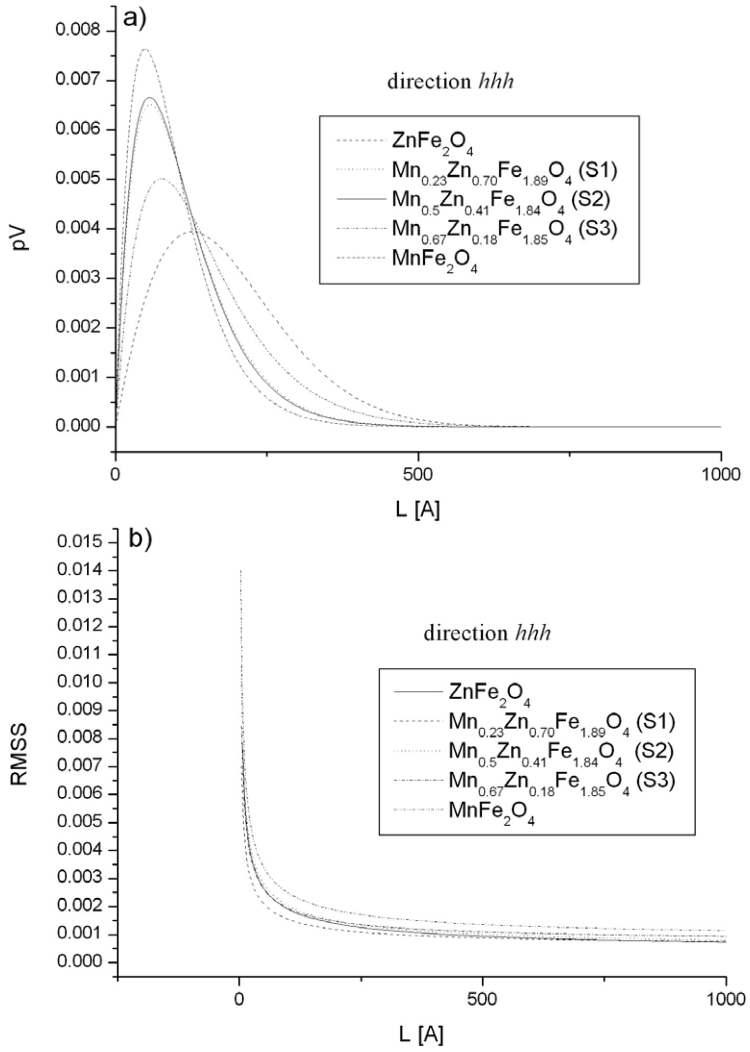

Figure 1. Crystallite size distribution (a) and RMSS strain distribution (b).

strain change non-systematically with the increase in Mn concentration. On an absolute scale there are discrepancies among these methods due to the different mathematical formalism regarding the description of the x-ray diffraction line broadening [14–20].

Comparing Warren–Averbach and simplified integral breadth methods it can be seen that the crystallite size and the strain, measured in the directions [111] and [110], are almost equal within experimental error. The parameter values, calculated in different directions, could be obtained from the refinement of the regular TCH–pV function, but the results could strongly depend on the correlation between refined FWHM parameters.

The domain size a_3', surface-weighted $\langle D\rangle_S$ and volume-weighted $\langle D\rangle_V$ crystallite sizes obtained by the Warren–Averbach method are different due to their different definitions [20]. The ratio $\langle D\rangle_V/\langle D\rangle_S$ is close to 2 for all the specimens presented in table 1. The RMSS over the distance $\langle D\rangle_V/2(\langle\varepsilon^2\rangle^{1/2}_{\langle D\rangle V/2})$, i.e. in the centre of the crystallite (obtained from

the Warren–Averbach method), is in good agreement with the upper limit of strain $\langle\varepsilon^2\rangle_{CC}^{1/2}$ (obtained from the simplified integral breadth method in the approximate Cauchy–Cauchy distribution of crystallites and strains). The RMSS over infinity ($\langle\varepsilon^2\rangle_{Gauss}^{1/2}$) is not in agreement (within the estimated errors) with the strains obtained from the simplified integral-breadth methods in the approximate Cauchy–Cauchy $\langle\varepsilon^2\rangle_{CC}^{1/2}$, Cauchy–Gauss $\langle\varepsilon^2\rangle_{CG}^{1/2}$ and Gauss–Gauss $\langle\varepsilon^2\rangle_{GG}^{1/2}$ distribution of crystallites and strains, although these values should be close. The best agreement is between ($\langle\varepsilon^2\rangle_{Gauss}^{1/2}$) and $\langle\varepsilon^2\rangle_{GG}^{1/2}$. The averaged values of apparent crystallite size and strain obtained by the refinement of the TCH–pV parameter value and the cubic harmonic function method are in good agreement. The crystallites obtained from the refinement of the TCH–pV parameter and cubic harmonic function methods are about 70% larger, while the strains are close to the values obtained from the Warren–Averbach and simplified integral breadth methods. Values in parentheses for crystallite size and strain represent the maximal deviation from the average value, and are a measure of the crystallite size and strain anisotropy.

3.1.3. Comparison of size–strain analysis methods. None of the methods applied for size–strain analysis is perfect. The integral breadth analysis is an oversimplification based on an arbitrary assumption of integral-breadth components due to size–strain effects (Cauchy–Cauchy, Cauchy–Gauss, etc). The Warren–Averbach analysis is based on the assuming of a TCH–pV profile function in FullProf. The refinement using cubic harmonics is arbitrary, too. This method applies symmetry conditions to the coefficients both for strain and for the size effects. While it is acceptable for the strain part (as we have used it), it is absolutely arbitrary for the size component. For the strain part, this model, even if it assumes symmetry restrictions compatible with the tensor properties, still deals with Cauchy and Gauss components of the line profile, thus *a priori* assuming a Voigtian profile shape.

The line profile parameters refined by the FullProf computer program are used as an input in the Breadth program. This means that the Breadth program does not use the original experimental data, but a representation in terms of Cauchy/Gauss profile components in the form of the TCH–pV profile function. As a consequence the results of the size–strain analysis are constrained by this hypothesis. The Warren–Averbach method is performed on experimental data and is a numerical method. The Breadth program constrains results to be compatible with the Voigtian profile. That is an arbitrary assumption. Among the different methods of x-ray line broadening analysis applied it seems that the cubic harmonic method is more precise and reliable than the Warren–Averbach and the simplified integral breadth methods for the following reasons: (i) the simultaneous refinement of structure (intensity dependent parameters) and microstructure (profile dependent parameters), (ii) the possibility of introducing symmetry constraints for the x-ray line broadening, (iii) the whole powder pattern refinement at the same time, and (iv) the precise and simultaneous separation of x-ray line broadening due to a strain or size effect for all reflections.

3.1.4. Particle shape and size versus crystallite size. In order to see the difference between crystallites and particles in the samples studied we analysed the particle shape and size distribution from the TEM micrograph (figure 2) for the ferrite S1. For the other specimens we assumed a similar difference between particles and crystallites. It seems that ferrite particles are more or less isometric, i.e. spherical. The particle distribution for sample S1 is in the range from 13 to 22 nm. This is close to values for the crystallite size (table 1). Hence, we can conclude that on average each particle consists of one crystallite. This conclusion is important for further discussion of the DC magnetization study in section 3.2.

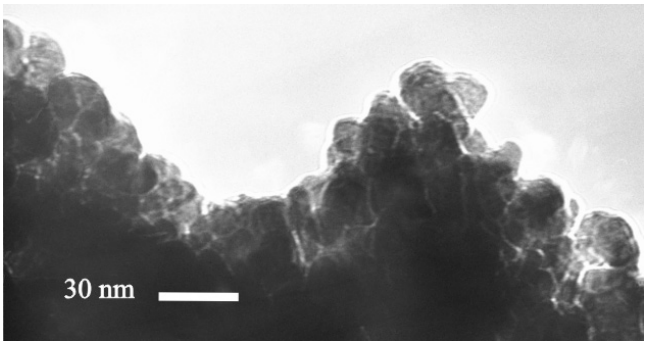

Figure 2. TEM microphotograph for S1 sample.

3.2. DC magnetization versus temperature

The temperature dependences of ZFC and FC magnetization for all the investigated samples measured in a field $H = 100$ Oe are shown in figure 3. The results are summarized in the following statements:

(i) ZFC and FC magnetization curves separate at the temperature of irreversibility T_{ir}, which is assumed to be a value above which $(M_{FC} - M_{ZFC})/M_{ZFC}$ is less than 1%. The irreversibility found, as well as the appearance of a maximum in ZFC magnetization at T_{max}, is typical of both the superparamagnetic (SPM) and the spin-glass (SG)-like state, where T_{ir} marks the starting point of the blocking or freezing temperature, respectively. Magnetization irreversibility was noticed in fields up to 1 kOe for sample S1. Namely, the $T_{ir} - T_{max}$ difference diminishes with increasing field, and disappears at applied fields of 1–1.5 kOe.

(ii) ZFC magnetization markedly decreases below T_{max}, while FC magnetization continues to increase below T_{ir} up to its maximum value and decreases afterwards (except for the Mn ferrite). Such magnetization behaviour is commonly ascribed to the presence of either interparticle dipole–dipole interaction or exchange coupling [21], unlike the constant increase of the FC branch that is observed for non-interacting particles [22]. Another possible reason for the observed shape of the FC branch is the temperature dependence of the anisotropy constant K [21]. In order to eliminate the difference in cooling/heating rate during the FC experiment as a possible non-physical reason for the appearance of the FC maximum [23], we performed additional measurements on sample S1 with a constant cooling/heating rate, but the same shape of the FC branch was obtained.

(iii) The value of T_{max} increases with the Mn content in the whole series of samples, except for the Mn ferrite. Many different factors influence the T_{max} value in a nanoparticle system, including structure- and microstructure-induced magnetic anisotropy, interparticle interactions (dipole–dipole or exchange coupling) and applied field. In the following text we consider the influence of several different types of anisotropy.

From the TEM micrograph, in the first approximation, it can be concluded that particles of sample S1 are spherical. Also, analysis based on cubic harmonic functions showed that the samples studied were composed of nearly spherically shaped crystallites [11]. Hence the shape anisotropy can be neglected. The presence of microstrain in the crystallites (table 1 and [11]), suggests that strain-induced anisotropy should be taken into consideration. As we found in [11], the x-ray line broadening due to the strain effect is significantly anisotropic. The anisotropy of x-ray line broadening is significantly higher in binary than in ternary samples.

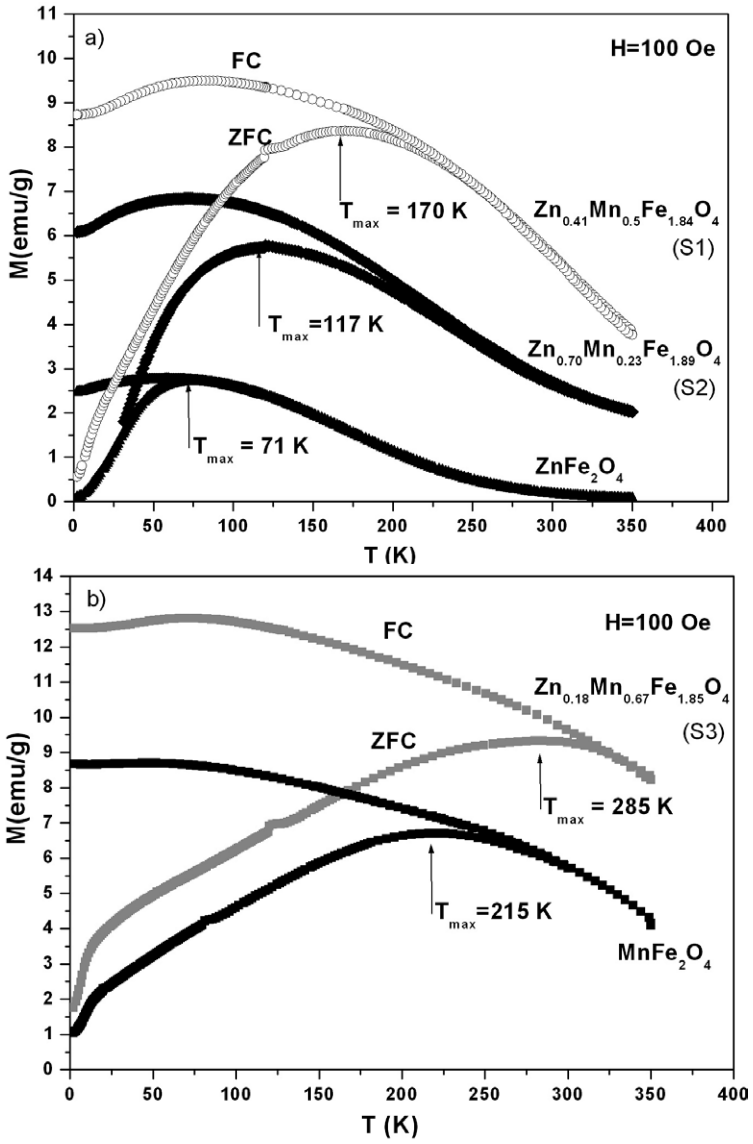

Figure 3. The temperature dependence on magnetization of the samples: (a) $ZnFe_2O_4$, $Zn_{0.70}Mn_{0.23}Fe_{1.89}O_4$ (S1) and $Zn_{0.41}Mn_{0.50}Fe_{1.84}O_4$ (S2) and (b) $Zn_{0.18}Mn_{0.67}Fe_{1.85}O_4$ (S3) and $MnFe_2O_4$, measured after ZFC and FC in applied field of 100 Oe.

As is known from the literature [24], the next factor that could influence the anisotropy energy, i.e. T_{max}, is the particle size; a larger particle induces a larger anisotropy energy and a higher blocking temperature. Therefore, a lower value of T_{max} in Mn ferrite than in sample S3 may be a consequence of different crystallites sizes; see table 1.

The crystalline anisotropy depends on the strength of the *L–S* interactions and the local crystal field. The strength of the *L–S* coupling is different in the studied samples, due to the differences in their chemical composition, stoichiometry and cation distribution. It was shown that ternary samples S1, S2 and S3 are cation-deficient (non-stoichiometric) spinels [11].

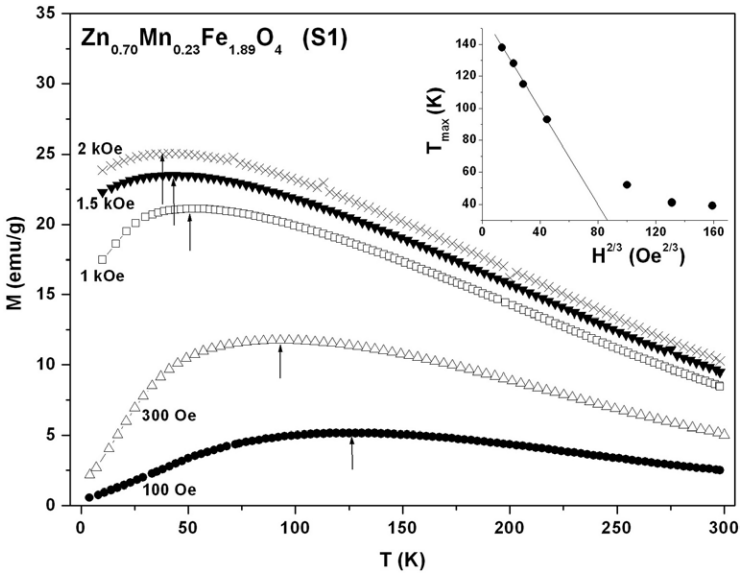

Figure 4. ZFC magnetization versus temperature at different fields (100 Oe–2 kOe). The arrows denote the temperature of magnetization maximum (T_{max}). The inset: T_{max} versus $H^{2/3}$. The line is a fit to the Almeida–Thouless (AT) line.

Non-stoichiometry in Zn–Mn ferrites is accompanied by a cation valence change, i.e. partial oxidation of Mn^{2+} to Mn^{4+} occurs. The percentage of Mn^{4+} in the samples was found to be S1 (84%), S2 (64%) and S3 (44%) [11]. The partial oxidation of Mn^{2+} to Mn^{4+} in ternary sample S3 is probably a significant factor in the above-mentioned T_{max} lowering in Mn ferrite. Regarding the cation distribution, it should be noticed that in all samples Zn^{2+} and Mn^{2+}/Mn^{4+} occupy exclusively tetrahedral sites, while Fe^{3+} cations are placed on octahedral sites [11]. Since the cation distribution is unchanged, it cannot be considered as a cause of the lower value of T_{max} in Mn ferrite (figure 3). Among other factors that influence the value of T_{max}, we will consider the existence of interparticle interactions and the influence of the applied field.

Further investigations of the nature of the magnetic state at lower temperatures involved $M(T)$ measurements in different applied fields (50 Oe–2 kOe) for sample S1. The ZFC dependences obtained are shown in figure 4, where arrows denote positions of T_{max}. Magnetization measurements in fields of 50 and 150 Oe were made in a narrow temperature region (60–170 K), and are not shown. A shift of the ZFC magnetization maximum to lower temperatures with the increase of the applied field can be easily noticed in figure 4, where a plot of the dependence of T_{max} versus $(H^{2/3})$ is also depicted (inset). It can be seen that T_{max} strongly increases with the lowering of magnetic field, and shows linearity versus $H^{2/3}$ at low fields. The full line represents the fit to the Almeida–Thouless (AT) line given by the relation $H_{AT}(T_{SG}) \sim [1 - (T_{SG})(H)/(T_{SG})(0)]^{3/2}$ [25], where $T_{SG}(H)$ is assumed to be $T_{max}(H)$ and $T_{SG}(0)$ denotes the freezing temperature at zero-field ($T_{max}(H = 0)$). Extrapolation of the AT line to $H = 0$ gives a value of $T_{SG}(H = 0) = 160$ K. Since AT dependence is widely accepted to be valid in spin-glass systems, we can consequently consider T_{max} as the temperature of spin-glass transition (i.e. the freezing temperature). The validity of the AT behaviour was found in many different systems in which interparticle exchange interactions are present: in canonical spin-glass systems, e.g. CuMn [26]; in amorphous bulk Fe_2O_3 [27]; in nanocrystalline Ni-

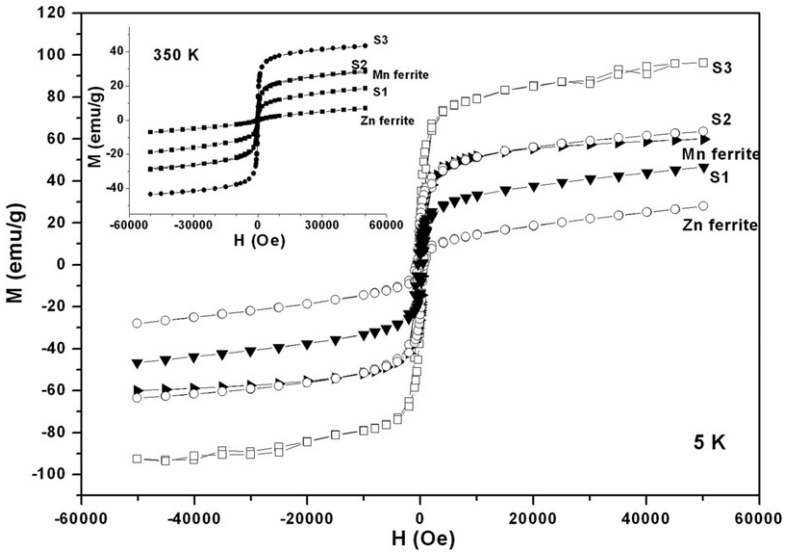

Figure 5. Hysteresis loops of the investigated samples measured at 5 K. The inset: hysteresis loops at 350 K.

ferrite with core/shell morphology of nanoparticles (where freezing of the spin-glass-like shell was considered) [28]; and in the nanoparticle spinel ferrite $Fe_{2.9}Zn_{0.1}O_4$ [29].

3.3. Hysteresis

The hysteresis loop of the investigated samples was measured at 5 K, figure 5. The obtained $M(H)$ curves are characterized by non-saturation of magnetization up to $H = 50$ kOe. The magnetization $M_{5\,\mathrm{K}}$ increases with the increase of manganese concentration for samples S1–S3, and then decreases for Mn ferrite. The same behaviour is already seen in figure 3. We consider non-stoichiometry accompanied with cation valence change (as was already discussed in analysis of $T_{\max}$ behaviour) as well as particle size as main causes for this behaviour. The magnetic moment of nanoparticles strongly depends on the particle size. Namely, the decrease in particle size increases the surface to volume ratio, and more magnetic ions located at the particle surface cause the surface uncompensated magnetic moments to become significant for the net magnetization.

Magnetization versus field at 350 K (shown in the inset of figure 5) is typical for SPM systems: up to 50 kOe magnetization does not saturate, and both remanence and coercivity are zero. In figure 6 are depicted obtained values of normalized magnetization, (M/M_{S} versus H/T) for S1 sample measured in the superparamagnetic region, i.e. at temperatures of 200 and 300 K. The saturation magnetization M_{S} is obtained by extrapolating the $M(1/H)$ dependence to the $1/H = 0$ value. It can be seen that magnetization curves do not coincide, so this could be an indication of the interparticle interactions.

To further investigate the existence of interparticle and intraparticle interactions, we measured hysteresis loops for sample S1 at different temperatures below $T_{\max}$. Measurements at each temperature were made in both the FC and ZFC regime. The hysteresis loops obtained in the FC/ZFC regimes at 2 K are shown in figure 7. Asymmetry of the magnetization loops in the FC regime, as well as a shift of FC branch with respect to the ZFC branch, may be observed. The $H_{\mathrm{C}-}(\mathrm{FC}) - H_{\mathrm{C}-}(\mathrm{ZFC})$ value is greater at lower temperature; see the

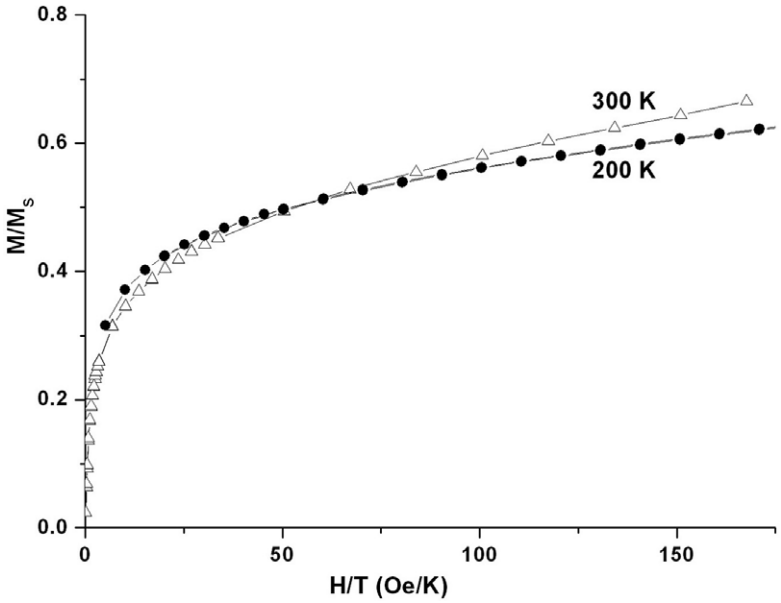

Figure 6. Normalized magnetization versus H/T for $Zn_{0.70}Mn_{0.23}Fe_{1.89}O_4$ at 200 and 300 K.

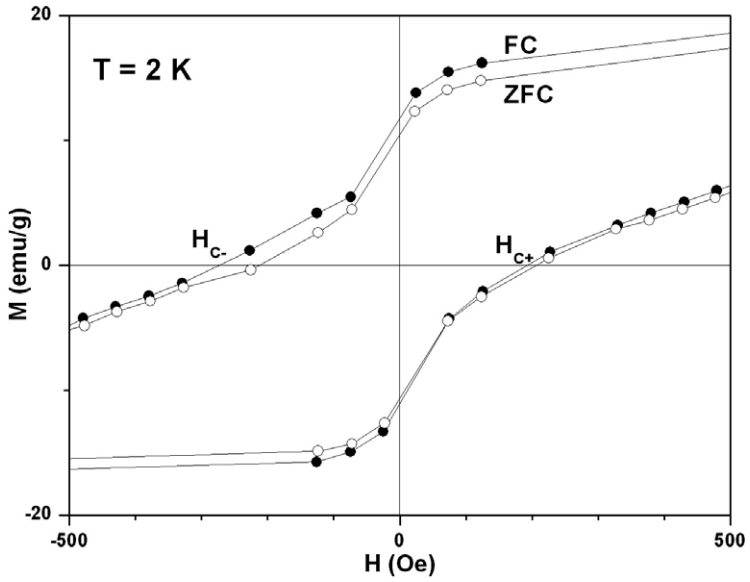

Figure 7. Hysteresis loops for $Zn_{0.70}Mn_{0.23}Fe_{1.89}O_4$ (S1) measured after FC and ZFC at 2 K (see text).

inset in figure 8. This value strongly decreases with increasing temperature in the region $2\ \mathrm{K} \leqslant T \leqslant 8\ \mathrm{K}$, remains nearly constant up to 40 K, and finally decreases to zero at 80 K. The observed results are commonly described by a core/shell structure of nanoparticles and spin-canting. In the core/shell model nanoparticles are assumed to consist of an ordered core and a disordered spin-glass-like shell. During field cooling a metastable surface spin configuration

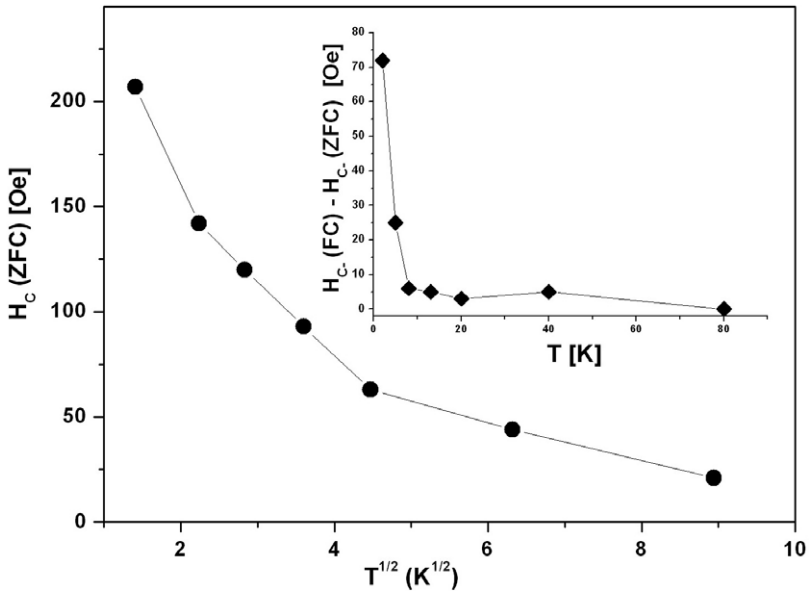

Figure 8. Variation of coercivity with temperature for $Zn_{0.70}Mn_{0.23}Fe_{1.89}O_4$ (S1). The inset shows the variation of loop shift.

is frozen, resulting in a net magnetic moment along the field direction. Exchange coupling between spins in the ordered core with those in the spin-glass-like shell produces an additional anisotropy term which makes the particle magnetic moment alignment along the field direction more favourable [30–33]. On the other hand, taking into account the observed structural and microstructural data (cation distribution, large concentration of vacancies, magnetic dilution and change in cation valence), the spin canting in nanoparticles is a possible cause of the hysteresis loop shift. Spin canting in spinel ferrites has been discussed; see, for example, [34]. The main difference between measurements reported in figure 3 and 7 is in applied field strength. $M(T)$ measurements were conducting in a constant low field of $H = 100$ Oe, while $M(H)$ measurements were done starting from a high field of 5 T. Hence, the magnetization difference $(M(\mathrm{FC}) - M(\mathrm{ZFC}))$ is small in $M(H)$ measurements (figure 7), while this difference is huge in $M(T)$ measurements (figure 3).

Magnetic anisotropy strongly affects the shape of hysteresis loops and controls the coercivity and remanence. Size/strain analysis has shown that strain-induced anisotropy is significant. Strain-induced anisotropy can cause unpredictable changes in magnetic properties. Consequently, the observed hysteresis shape (figure 7) could also be induced by strain.

The change of H_C(ZFC) with temperature is presented in figure 8. H_C decreases with increasing temperature, as could be expected. In non-interacting nanoparticle ensembles, the $H_C(T)$ dependence should obey the relation $H_C = H_{C0}[1 - (T/T_B)^{1/2}]$ [22]. The observed deviation in linearity of the $H_C(T^{1/2})$ curve is also attributed to the existence of interparticle interactions.

Further, we considered the reduced remanence M_R/M_S of S1. The theoretical M_R/M_S value of 0.5 for non-interacting single-domain particles with the easy axis randomly oriented was found experimentally in some non-interacting nanoparticle systems, e.g. in Co ferrite [31]. Lowering of this value could be induced by internal strain [35]. A ratio of 0.15 at 5 K was reported for Fe_3O_4 with interparticle interactions [32]. The value $M_R/M_S(2\ \mathrm{K}) = 0.2$ obtained

for sample S1 is probably induced by both internal strain and interparticle interactions. This is another confirmation that the ferrites studied consist of interacting nanoparticles.

The results of DC magnetization measurements suggest a picture of interacting ferrite nanoparticles with interparticle interactions comparable to or greater than the magnetic anisotropy energy, E_A. Probably, single-domain nanoparticles ('superspins') undergo collective freezing below $T_{max} \equiv T_{SG}$. Consequently, a phase transition from interacting superparamagnetic (SPM) to super spin-glass (SSG) state at T_{max} occurs in the investigated ferrites.

4. Conclusion

To analyse the microstructural parameters (crystallite size and strain) both the Warren–Averbach and simplified integral breadth methods were applied. The results were compared with those obtained from the cubic harmonic function method. It seems that the cubic harmonic method is more precise and reliable than the Warren–Averbach and simplified integral breadth methods. Transmission electron micrography indicated that the particle size is on average the same as the crystallite size. Therefore we can conclude that these ferrites are composed of single-domain particles. DC magnetization measurements, ZFC and FC magnetization at different temperatures and applied fields, as well as $M(H)$ at different temperatures, all indicate that the particles show superparamagnetic behaviour, even above room temperature. The shift in hysteresis loops is explained by the core/shell morphology of nanoparticles and spin canting. Reported dependences of $T_{max}(H)$, $H_C(T)$ and M_R/M_S versus H/T, as well as the maximum in FC magnetization, confirm the existence of interparticle interactions. The structural and microstructural data found allowed a discussion of magnetic parameters such as T_{max}, magnetization values and M_R/M_S ratio. The lower value of T_{max} in Mn ferrite compared to that in sample S3 is probably a consequence of both different crystallite size (table 1) and the established non-stoichiometry accompanied by the valence change (Mn^{2+} to Mn^{4+}). The AT line obtained shows the characteristics of a spin-glass system, so T_{max} could be attributed to the freezing temperature.

Acknowledgments

This work was financially supported through the joint project 'Synthesis and physical properties of nanosize and polycrystalline magnetic materials', supported by the Serbian Ministry of Science and Environmental Protection and the Slovenian Ministry of Science, as well as by project No. 2022 of MNZZS. We thank Igor Peterka for performing the TEM measurements.

References

[1] Kodoma R H, Berkowitz A E, McNiff E J and Foner S 1996 *Phys. Rev. Lett.* **77** 394
[2] Kodoma R H 1999 *J. Magn. Magn. Mater.* **200** 359
[3] Tronc E *et al* 2003 *J. Magn. Magn. Mater.* **262** 6
[4] Néel L 1949 *Ann. Geophys.* **5** 99
[5] Sasaki M, Jönsson P E, Takayama H and Mamiya H 2004 *Preprint* cond-mat/0406546
[6] Sahoo S, Petracic O, Binek Ch, Kleemann W, Sousa J B, Cardoso S and Freitas P P 2002 *J. Phys.: Condens. Matter* **14** 6729
[7] Herbst J F 1991 *Rev. Mod. Phys.* **63** 819
[8] Novakova A A, Lanchinskaya V Yu, Volkov A V, Gendler T S, Kiseleva T Yu, Moskvina M A and Zezin S B 2003 *J. Magn. Magn. Mater.* **258/259** 354
[9] Vestal C R and Chang Z J 2002 *Chem. Mater.* **14** 3817

[10] Topfer J, Liu L and Dieckmann R 2003 *Solid State Ion.* **159** 397
[11] Antic B, Kremenovic A, Nikolic A S and Stoiljkovic M 2004 *J. Phys. Chem.* B **108** 12646
[12] Tanaka T 1978 *Japan. J. Appl. Phys.* **17** 349
[13] Kang S-H and Yoo H-L 2000 *J. Appl. Phys.* **88** 4754
[14] Balzar D 1992 *J. Appl. Crystallogr.* **25** 559
[15] Balzar D 1993 *J. Res. Natl Inst. Stand. Technol.* **98** 321
[16] Klug P H and Alexander E L 1974 *X-ray Diffraction Procedures for Polycrystalline and Amorphous Materials* (New York: Wiley) p 618
[17] Louër D and Langford I J 1988 *J. Appl. Crystallogr.* **21** 430
[18] Järvinen M 1993 *J. Appl. Crystallogr.* **26** 525
[19] Honkimäki V and Surotti P 1999 Effects of instrument function, crystallite size, and strain on reflection profiles *Defect and Microstryctyre Analysis by Diffraction* (*IUCr Book Series*) (New York: Oxford University Press) p 41
[20] Warren B E 1969 *X-ray Diffraction* (Reading, MA: Addison-Wesley) p 251
[21] Tung L D *et al* 2002 *Physica* B **319** 116
[22] Fonseca F C *et al* 2002 *Phys. Rev.* B **66** 104406
[23] Dey S, Roy A, Ghose J, Bhowmik R N and Ranganathan R 2001 *J. Appl. Phys.* **90** 4138
[24] Mukadam M D, Yusuf S M, Sharma P and Kulshreshtha S K 2004 *J. Magn. Magn. Mater.* **272–276** 1401
[25] Almeida J R L and Thouless D J 1978 *J. Phys. A: Math. Gen.* **11** 983
[26] Kenning G G, Chu D and Orbach R 1991 *Phys. Rev. Lett.* **66** 2923
[27] Mukadam M D, Yusuf S M, Sharma P and Kulshreshtha S K 2004 *J. Magn. Magn. Mater.* **269** 317
[28] Martinez B, Obradors X, Balcells L, Rouanet A and Monty C 1998 *Phys. Rev. Lett.* **80** 181
[29] Chander S, Kumar S, Krishnamurthy A, Srivastava B K and Aswal V K 2003 *Pramana—J. Phys.* **61** 617
[30] Cannas C *et al* 2001 *Phys. Chem. Chem. Phys.* **3** 832 and references therein
[31] Tung L D, Kolesnichenko V, Caruntu D, Chou N H, O'Connor J and Spinu L 2003 *J. Appl. Phys.* **93** 7486
[32] Goya G F, Berquó T S, Fonseca F C and Morales M P 2003 *J. Appl. Phys.* **94** 3520
[33] Muroi M, Street R, McCormick P G and Amighian J 2001 *Phys. Rev.* B **63** 184414
[34] Jiang J Z, Goya G F and Rechenberg H R 1999 *J. Phys.: Condens. Matter* **11** 4063
[35] Ammar S *et al* 2001 *J. Mater. Chem.* **11** 186